Journal of Energy and Environment Technology ISSN 2392-5701

http://jeet.siamtechu.net Research Article

EFFECT OF ENERGY AND ENVIRONMENT ON WELDED JOINTS BETWEEN SS304 AND Q245 USING GTAW

Kanok-on Rodjanakid[1*] Nutthapong Kunla[1] Sonthaya Khamdech[1] Anusorn Phongprapa[1]

[1]*Division of Mechanical Engineering, Faculty of Engineering, BangkokThonburi University, 10170*

[*]*Corresponding author Email : kanok-on.rodj@gmail.com*

Received: August 16, 2025

Revise: November 29, 2025

Accepted: December 12, 2025

Abstract

This research aims to study the effect of energy and environment on welded joints of SS304 and Q245 steel of gas tungsten arc welding (GTAW) using filler metal AWS A5.9: ER309L. The specimen dimension was 150 × 100 mm with a thickness of 6 mm. The results of the experiment found that characteristics of deep penetration and melting between the weld metal and consistent metal work and there is perfection between the weld metal and the base metal. The welding GTAW technique process will produce an average maximum tensile strength of 463.64 MPa. The maximum hardness in the heat effected zone (HAZ SS304) is 182 HV and the lowest hardness in the base metal zone (HAZ SS304) is 130 HV. The microstructure structures of the weld zone consist of dendrite ferrite and austenite matrix, which resulted in the heat affected zone will have higher hardness than the base metal. Temperature results obtained from the infrared thermometer and numerical simulation different of 5% which is an acceptable value. The summary result, it can be concluded that the gas tungsten arc welding (GTAW) uses less energy than the shielded metal arc welding (SMAW) due to the lower heat consumption, but produces higher quality and cleaner results. Environmentally, GTAW welding has a lower impact than SMAW welding, particularly in terms of smoke and slag generation, making it more environmentally friendly.

Keywords: Gas tungsten arc welding, Metallurgical, Mechanical properties, Numerical simulation

1. Introduction

Modern welding processes require a greater variety of methods to achieve the desired objectives of specific applications. Welded construction between carbon steels and stainless steel is widely used in chemical, petroleum, natural gas, nuclear energy and power generation sectors, and exhibits advantages, such as low cost for carbon steels and good corrosion resistance for stainless steels [1]. Generally, welding is done using shielded metal arc welding (SMAW) welding method because it is convenient for field work. To select the appropriate welding process for joining the two types of materials, as shown in Figure 1, gas tungsten arc welding (GTAW), which is characterized by its high controllability and low equipment cost, is widely used for precision sheet metal welding. Also known as tungsten inert gas (TIG) welding, it is a well-known welding technique for a wide range of materials [2]. The gas tungsten arc welding (GTAW) is also less energy-efficient than the shielded metal arc welding (SMAW) due to its lower heat consumption, yet it produces higher quality and cleaner results. GTAW welding has a lower environmental impact than SMAW welding, especially in terms of fumes and slag generation, making it more environmentally friendly. However, SMAW welding is still a widely used welding process, especially in maintenance and field applications, where it is more convenient than GTAW welding [3].

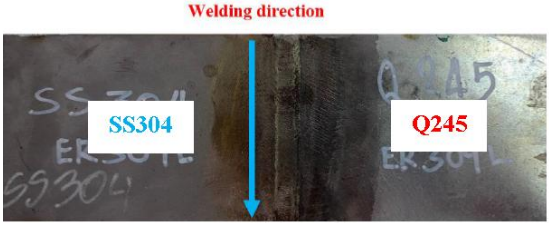

Figure 1 The specimens of SS304 and Q245 welded by gas tungsten arc (GTAW) method

Several studies have focused on analyzing metallurgical, mechanical properties, and the thermal effects associated with welding joints Himanshu Vashishtha studied the mechanical properties and microstructure of dissimilar welding between AISI 201 and AISI 304 for GTAW and SMAW processes [4]. The experimental results showed that at welding speeds of 2 mm/s and 2.7 mm/s, the welds were successfully obtained via the GTAW process. In addition, in the heat affected zone, there were smaller dendritic components obtained from the high welding speed, which resulted in an increase in the microstructure hardness and better weld metal tensile strength for the GTAW process. Chang' an Li studied the base metal of stainless-steel clad plates filled with carbon steel filler metal, and the microstructures and mechanical properties of joints with diverse filler metals were analyses and compared [5]. The results indicate that a local hardening zone (LHZ) forms in the weld filled with filler metals of stainless steel and carbon steel because of the formation of martensite phase in the first layer of weld with filler metal of carbon steel. The results of the side bending test indicate that the LHZ protrudes from the weld, and the crack occurs near the LHZ if the area of the LHZ on the cross section of joint is larger than 17 % of that of the whole cross section of the joint. Mehran Ghafouria studied the welding distortions, temperature measurement and solid-state phase transformation of ultra-high strength steel S960 [6]. The experimental results show that the simulation predicts that the welded materials in HAZ and FZ have a bainite-martensite microstructure, in which martensite has a smaller share than bainite. Comparison between the prediction of angular distortion caused by welding and out-of-plane bending deformation using SSPT model shows higher accuracy level. I. Reda Ibrahim examined the mechanical properties in dissimilar butt joints between Ni medium manganese and nickel-chromium austenitic stainless steels processed by GTAW [7]. The experimental results showed that the microstructure consisted of austenite and delta ferrite matrix obtained by welding dissimilar butt joints. It was also found that the weld still has a low tensile strength value at 610 MPa, which is lower than the base metal (BM) M-Mn SS and Ni-Cr SS. The cause is due to the uneven dendritic structure of the weld zone where Cr-carbide precipitation occurs. C-H Huang [8] investigated mechanical and corrosion properties of dissimilar welded joints between SUS304 stainless steel and SS400 low carbon steel. The experimental results showed that the microstructure around the weld and SUS304 showed more granular corrosion and corrosion bumps as the immersion time increased. The samples were immersed in sodium chloride solution for 21 days, and the EDS results showed a decrease in chromium content, which led to increased corrosion. Mahmoud Khedr examined mechanical properties and microstructure of two joints of Medium-Mn stainless steel with Low-and High-alloyed steel using the gas tungsten arc welding technique [9]. The microstructure in the weld zone was found to be mainly composed of austenite matrix and a small fraction of ferrite (3.5~5.7%). The tensile stress of MMn–SS/NiCr–SS welds was higher than that of MMn–SS/LCS welds, with values of 610 and 340 MPa, respectively. Jinkamon Luijan investigated ER308L and ER309L filler metal on dissimilar metals between carbon steel and 3CR12 ferritic stainless steel using the gas tungsten arc welding technique [10]. The results of using ER308L welding wire at 70A welding current revealed that the microstructure consisted of delta ferrite and austenite, and when compared with 100A welding current, delta ferrite, austenite and martensite were present. In addition, no carbide formation was found in the weld metal zone when using ER308L welding wire. The delta ferrite content was higher than that of ER309L welding wire, and the delta ferrite content increased with increasing hardness.

Abdulrahaman Shuaibu Ahmad analyses the residual stress and deformation field induced by double-pass TIG welding of Al 2219 plate [11]. The FE model was developed using ABAQUS and FORTRAN packages utilising Goldak's ellipsoid heat source model. The FE model was experimentally validated, and the compared results show good agreement with average variations of 18.8% and 17.4% in residual stresses and deformation, respectively. S. Nuchim examined residual stress and distortion in Thermo-Mechanical Control Process (TMCP) grade EH-36 steel plates of butt joints welding by hybrid GTAW and SMAW process [12]. The thermal measurements show a close agreement between the experimental and numerical simulation thermocouple data, with a temperature deviation of only 5%. Residual stress analysis using X-ray diffraction reveals that ultrasonic stress relaxation reduces the maximum residual stress from an average of 193.4 MPa to 39.1 MPa. Distortion analysis shows that the maximum FEM deformation is 0.2873 mm, with a deviation of 12% from the coordinate measurement (CMM) results, while the minimum FEM deformation is 0.031922 mm, a difference of 3%. Saulius Baskutis study utilized a metal inert gas welding (MIG) to make a dissimilar weld of stainless steel AISI 304, 314, 316L, 420 grades and a standard structural steel S355MC [13]. The results obtained of welds in all grades of austenitic steels can withstand tensile tests with an average tensile strength of 472 MPa. In addition, cracking was detected in the base metal zone, indicating that the use of 308LSI filler metal is only suitable for welding austenitic stainless steels and dissimilar structural steels and is not suitable for welding martensitic structural steels.

This research aims to study the effects of gas tungsten arc welding with AWS A5.9: ER309L filler metal on SS304 and Q245 by performing macro and microstructural analysis, tensile test, hardness measurement, measuring the alloying elements in the weld line using EDS (Energy dispersive spectroscopy) technique and thermal analysis. Finally, the experimental results are analyzed and summarized.

2. Welding Procedure and Experiment

2.1 Welding materials

In this welding of dissimilar materials SS304 and Q245 steel plates were selected, dimensions of width 100 mm, length 150 mm, thickness 6 mm. The first plate is SS304 stainless steel with chemical composition as shown in Table 1. The second plate was Q245 steel with chemical composition as shown in Table 2.

Table 1 Chemical composition of SS304 (%wt)

Materials	SS304
C	≤ 0.080
Mn	≤ 2.00
Si	≤ 0.75
P	≤ 0.045
S	≤ 0.030
Cr	18.0 – 20.0
Ni	8.0 – 10.5
N	≤ 0.10

Table 2 Chemical composition of Q245 (%wt)

Materials	Q245
C	≤ 0.20

Mn	0.5 – 1.0
Si	$\leq$ 0.35
P	$\leq$ 0.025
S	$\leq$ 0.015
Al	$\leq$ 0.020

2.2 Filler metal

The filler metal used was AWS A5.9: ER309L, a diameter of 2.4 mm. with the chemical composition shown in Table 3. Figure 2 shows the welding process using (GTAW) according to AWS D1.1 standards.

Table 3 Chemical composition of ER309L (%wt)

Filler metal	AWS A5.9: ER309L
C	$\leq$ 0.030
Si	0.3 – 0.65
Mn	1.0 – 2.5
P	$\leq$ 0.030
S	$\leq$ 0.030
Ni	12 – 14
Cr	23 – 25
Mo	$\leq$ 0.75
Cu	$\leq$ 0.75

Figure 2 Gas tungsten arc welding process (GTAW)

2.3 Workpiece preparation and welding process

Preparation of the workpiece for welding was performed by creating a V-groove joint at an angle of 60 degree as shown in Figure 3. The welding process using gas tungsten arc welding (GTAW) in the 6G welding position by specifying the welding parameters as shown in Table 4. For welding processes using tungsten filler metal arc to generate heat and gas tungsten arc welding (GTAW), shielding gas during welding uses argon gas. The shielding gas flow volume can be set using a flow meter installed at the tank head, which can adjust the gas flow volume as needed. The welder will control the welding speed. For this experiment the speed is 13.7 mm/min which is related to the welding current. If high welding current is used and welding speed is set to increase, it will affect the quality of production. The amount of heat entering the weld line no matter whether it's a lot or a little will affect the properties of the weld line and HAZ such as hardness and tensile strength, etc. However, only 60% of the heat entering the weld line comes from TIG welding using Argon gas to cover it. Some of the heat from the arc is lost to the flow of gas, as well as radiation and other factors.

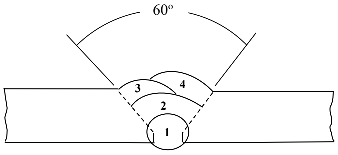

Figure 3 Standard requirements for welding procedure

Table 4 Welding parameters used in GTAW process

Parameter	Unit
Electrode diameter	2.4 mm
Arc Voltage	120 Volt
Current intensity	14 A
Welding speed	13.7 mm/min
Shielding gas flow volume	16 liters/min

2.4 Metallurgical and EDS Techniques

The metallographic examination was performed using an Olympus OLS 4000 laser microscope, as shown in Figure 4 which captured detailed images of the workpiece in 3D with high resolution. The welds were treated to study the weld characteristics and phase changes structures of SS304 stainless steel (Base metal: BM1), heat-affected zone 1 (HAZ1) of SS304 stainless steel, weld metal zone (WM), heat-affected zone 2 (HAZ2) of Q245 steel, and base metal 2 of Q245 steel (BM2). In addition, the chemical composition was examined using EDS (Energy dispersive spectroscopy) technique using a Scanning Electron Microscope (SEM) model JOEL: JSM-7800F prime, which was used to analyze the chemical composition of the elements in the weld metal zone.

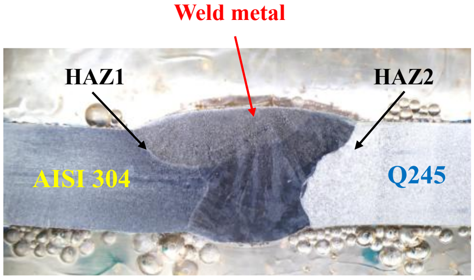

Figure 4 Position of metallurgical structure inspection in the specimen

2.5 Tensile test

Tensile testing using a universal testing machine, as shown in Figure 5. INSTRON model 8801, which is a longitudinal tensile testing machine for materials, prepared the specimens for tensile testing. The test parameters can be directly input from the touch screen. The test processing is in the form of numbers and graphs. In this research, this test is used to determine the yield strength, the ultimate tensile strength and percent elongation of the weld metal. The specimens were prepared for tensile testing according to ASTM E8/E8M-22 standard, as shown in Figure 6.

Figure 5 Universal testing machine model INSTRON: 8801

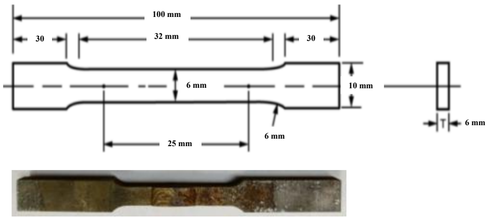

Figure 6 Preparation of specimens for tensile testing according to ASTM E8/E8M-22 standards

2.6 Hardness measurement

The hardness test was performed using Vicker hardness tester model SHIMADZU: HMV-G. The hardness values will be measured in various areas of the weld, such as the base metal, the heat affected zone (HAZ), and the weld metal as shown in Figure 7. The test was performed according to ASTM E3-11 standard using a force of 200 kgf (HV0.2 (1.961N) and a holding time of 15 seconds. The compression was started in the 2 lines, the top and bottom line of the GTAW welding pass.

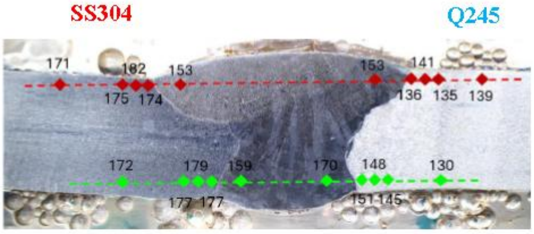

Figure 7 Area of hardness test points in the specimen

2.7 Thermal analysis

Using the assumptions described above, the conservation equations can be formulated. In a stationary, orthogonal curvilinear coordinate system (*x, y, z*) [11], the three-dimensional heat-transfer equation governing the time-dependent formation of solid material can be written as follows:

$$\frac{\partial}{\partial x_i}\left(k_{x_i}\frac{\partial T}{\partial x_i}\right)+Q=\rho c\frac{\partial T}{\partial t} \tag{1}$$

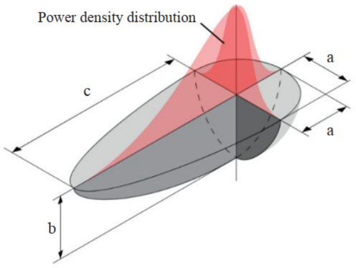

Figure 8 Three-dimensional shape of the heat source [11]

Where ρ denotes the mass density, c the specific heat capacity, and kx_i the components of the thermal-conductivity tensor. Q represents the applied heat input, while a, b and c correspond to the lengths of the ellipsoidal axes in the x, y, and z directions, respectively, as illustrated in Figure 8. T describes the temperature variation as a function of the axial coordinate x_i and time t, and x_i indicates the principal spatial axis. Based on these definitions [11], the stress relationship can be expressed as:

$$\sigma_{ij} = \lambda\delta_{ij}e + 2G\varepsilon_{ij} - (3\lambda + 2G)\delta_{ij}\alpha(\mathrm{T} - \mathrm{T}_0) \tag{2}$$

where σ_{ij} is the stress tensor, T_0 is the reference temperature at zero stress, α is the expansion coefficient, ε_{ij} is the strain tensor, and δ_{ij} is equal to 1 when $i = j$ or $i \neq j$.

$$\lambda = \frac{\nu E}{(1+\nu)(1-2\nu)}, \quad G = \frac{E}{2(1+\nu)}, \quad e = \varepsilon_{11} + \varepsilon_{22} + \varepsilon_{33} \tag{3}$$

where ν is the Poisson's ratio, and E is the modulus of elasticity.

According to the double-ellipsoid heat-source model, the source is divided into front and rear halves, each with its own heat-flux distribution [11]. The model uses Goldak's volumetric heat-flux formulation, where the heat flux in the front and rear regions is defined by equations (4) and (5), respectively.

For the front heat source,

$$q(x,y,z) = \frac{6\sqrt{3} f_f \eta VI}{abc_f \pi\sqrt{\pi}} e^{-3x^2/a^2} e^{-3y^2/b_f^2} e^{-3z^2/c^2} \tag{4}$$

and for the rear heat source,

$$q(x,y,z) = \frac{6\sqrt{3} f_r \eta VI}{abc_r \pi\sqrt{\pi}} e^{-3x^2/a^2} e^{-3y^2/b_f^2} e^{-3z^2/c^2} \tag{5}$$

where V is the voltage during welding, I is the arc current, and η is the arc efficiency with $b_f = a$, $b_r = 4b_f$, and $f_f + f_r = 2$; b_f is the distance of the front heat flux, b_r is the distance of the rear heat flux [10]. The geometric parameter a, b_f, b_r and c are schematically. The relationship between these heat-deposited fractions and geometric parameters is as below [11]:

$$f_f = \frac{2b_f}{(\mathrm{b}_f + b_r)} \tag{6}$$

$$f_f = \frac{2b_r}{(\mathrm{b}_f + b_r)} \tag{7}$$

The front half of the source corresponds to a quadrant of one ellipsoidal emitter, while the rear half corresponds to a quadrant of a second ellipsoidal emitter. The figure also illustrates the resulting power-density distribution along the y-axis [11].

Temperature measurement of welding used an infrared thermometer, FLUKE model 62 MAX to the side surfaces of the parent material. The positions at which the 4 points were measured are schematically the heat source location along from the weld centerline as shown in Figure 9. The numerical thermal simulation of the welded SS304 stainless steel and Q245 steel was performed using a 3D model as shown in Figure 10. The plate dimensions were 100 mm wide, 150 mm long and 6 mm thick. The coordinate system of the model and the mesh division consisted of the total number of elements = 3652, the total number of nodes = 6161 and the number of DOF = 6078. To ensure accuracy and minimize the error, 3-time numerical simulations were conducted with different numbers of elements [12]. Finally, the configuration giving the smallest error was selected. Due to the symmetry of the weld sample, only half of the weld was analyzed using the centerline of the weld as the axis of symmetry. The heat transfer data from the simulation were measured at four positions T_1, T_2, T_3 and T_4 on the weld model at time intervals of 150 and 450 s. These positions included the positions of the heat source at the centerline of the weld at distances of 12, 18 and 30 mm from the centerline as shown in Figure 11.

Figure 9 Measuring temperature on the surface of the workpiece with an infrared thermometer

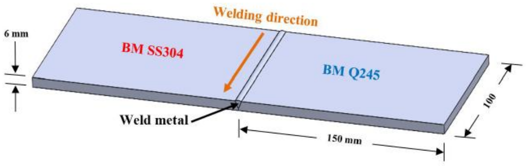

Figure 10 Three-dimension model

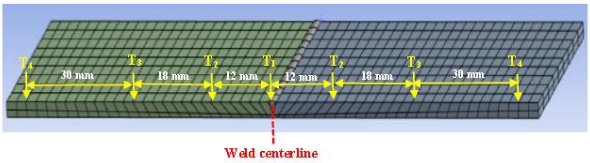

Figure 11 Heat transfer position

3. Result and discussion

3.1 Metallurgical and EDS Techniques

Microstructural examination by optical microscope (OM) as shown in Figure 12 the base metal zone of SS304 stainless steel (Base metal: BM1) at a magnification of 500x, 50 µm. The microstructure is generally a twin-phase austenitic stainless steel [5]. Figure 13 is an image of the heat affected zone (HAZ1) of SS304 stainless steel at a magnification of 100x, 200 µm. The microstructure of both weld metals consists of primary ferrite dendrites with interdendrite austenite. Interestingly, both have relatively high delta ferrite content [7], probably because of low carbon content of both filler metals in the weld in this work, which is consistent with the role that carbon tends to play in stabilizing the austenite phase in the weld metal.

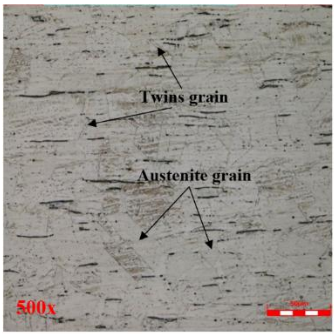

Figure 12 Microstructure in the base metal zone of SS304 stainless steel (Base metal: BM1)

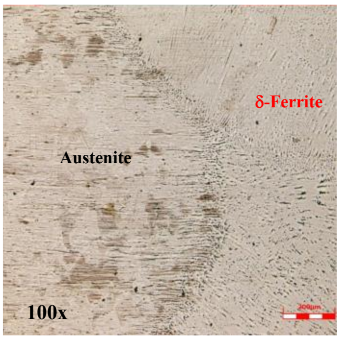

Figure 13 Microstructure in the heat affected zone (HAZ1)

Figure 14, The microstructure in the weld metal (WM) at 100x, 200 µm, consists of ferrite dendrite and austenite matrix [5, 7]. The chemical composition was also examined by EDS (Energy dispersive spectroscopy) technique using scanning electron microscope (SEM). The results of the analysis revealed that most of the elements are components of the welding wire with chromium as the highest content. The details of other elements are shown in Table. 5

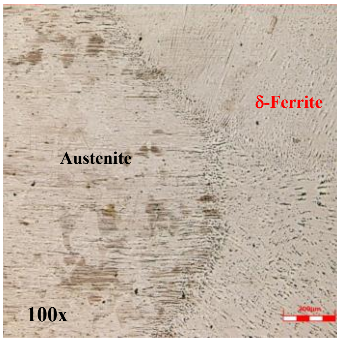

Figure 14 Microstructure in the weld metal zone (WM)

Table 5 Chemical composition of weld metal zone

Element	%wt
Cr	21.59
Ni	10.17
Fe	66.31
Mn	1.93

Figure 15 shows the heat affected zone (HAZ2) of Q245 steel at a magnification of 500x, 50 μm. The microstructure is generally composed of ferrite and pearlite, with pearlite distributed on the grain boundaries of the ferrite [5]. Figure 16 is an image of the base metal area of Q245 steel (Base metal: BM2) at 1000x, 40 μm. The microstructure is generally composed of ferrite and pearlite, with pearlite distributed on the grain boundaries of the ferrite [5].

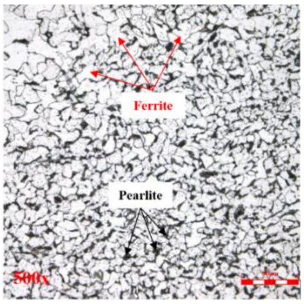

Figure 15 Microstructure in the heat affected zone (HAZ2)

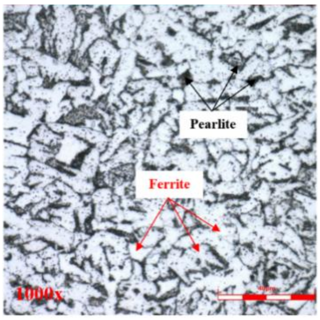

Figure 16 Microstructure in the base metal zone of Q245 steel (Base metal: BM2)

3.2 Tensile test

The tensile test results from the stress-strain curves of the welded specimens in Figure 17 show that all stresses have close values due to fracture of the specimens resulting from the tensile test. However, it was also found that all fractures occurred in the base metal Q245, especially at the HAZ, as shown in Figure 18. Therefore, it can be concluded that the most fragile part of the welded specimens is the base metal Q245 as shown in Table 6 [5, 7, 9, 13].

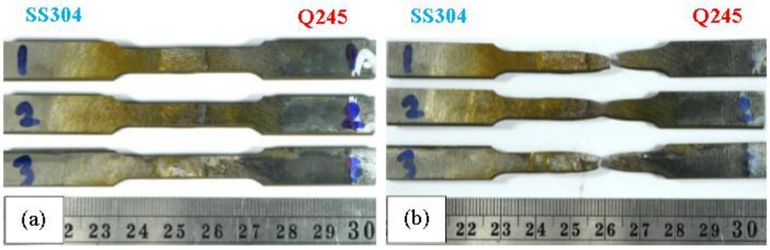

Figure 17 Tensile test specimen (a) before tensile testing (b) after tensile testing

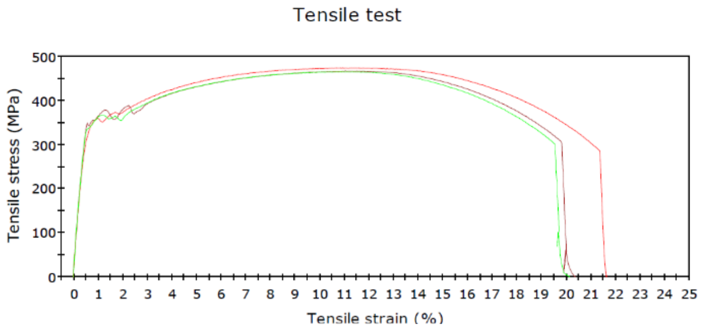

Figure 18 Stress-strain curves of the 3 specimens

Table 6 Tensile test results

No.	Yield strength (MPa)	UTS (MPa)	Elongation %	Location of fracture
1	333.84	463.85	20.59	BM Q245
2	337.28	457.12	19.59	BM Q245
3	338.82	469.95	18.97	BM Q245
Average	336.65	463.64	19.72	BM Q245

3.3 Hardness measurement

The results of the hardness test from the GTAW welding process are shown in Figure 19. The hardness profile of the weld is divided into 5 zones: base metal (BM SS304), heat affected zone (HAZ SS304), weld metal (WM), heat affected zone (HAZ Q245) and base metal (BM Q245). The trend of hardness value in each area of all 10 points along line 1 (Red line), it was found that the highest hardness value was at point 3, the heat effected zone is 182 HV, and the lowest hardness value was at point 9 is 135 HV. The heat effected zone (HAZ SS304) from test points 2-4 had a slightly higher hardness value than the weld metal (WM) at points 5-6 but had a higher hardness value than the heat effected zone (HAZ Q245) at points

7-9 [5, 7, 9, 13]. The trend of hardness value in each area of all 10 points along line 2 (Green line), it was found that the highest hardness value was at point 3, the heat effected zone is 179 HV, and the lowest hardness value was at point 10 is 130 HV. The heat effected zone (HAZ SS304) from test points 2-4 had a slightly higher hardness value than the weld metal (WM) at points 5-6 but had a higher hardness value than the heat effected zone (HAZ Q245) at points 7-9 [5, 7, 9, 13].

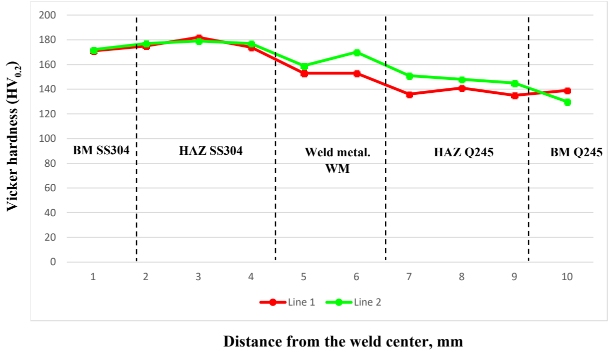

Figure 19 Hardness profile showing hardness of the weld metals and both sides

From the experiment, it was found that the weld metal when heated from welding causes the structure to change into a solid structure, therefore resulting in an increase in the hardness value. And the welding process in the heat effect zone next to the base metal area will have a harder value than the weld metal but will be higher than the base metal and will give the same results for both test point compression lines.

3.4 Thermal analysis

The temperature measurements taken while welding sheet metal pieces with an infrared thermometer measuring device were at follows position T_1 reached 327 °C, position T_2 recorded 280 °C, position T_3 measured 170 °C, and position T_4 showed 138 °C. Figure 20 illustrates the results of the thermal simulation, depicting the temperature distribution on the plate from the numerical simulation performed 3 times. Temperature at position T_1, located at the weld centerline center line, reached a peak of 309.63 °C. Uneven cooling due to convection and radiation caused a rapid decrease in temperature after the heat source moved past the location. For the subsequent positions, position T_2 showed 274.04 °C, position T_3 showed 167.28 °C, and position T_4 showed 131.69 °C. The heat generated during welding was transferred to the lower-temperature regions of the plate by conduction, while heat was dissipated into the environment through radiation and convection [11, 12]. When comparing the results of infrared thermometer measurements and numerical simulations gives temperature values that are not significantly different at 5% difference, which is an acceptable value. Meanwhile, the results also show that the heat distribution characteristics of the temperature are similar to the research of Abdulrahaman Shuaibu Ahmad et al [11, 12].

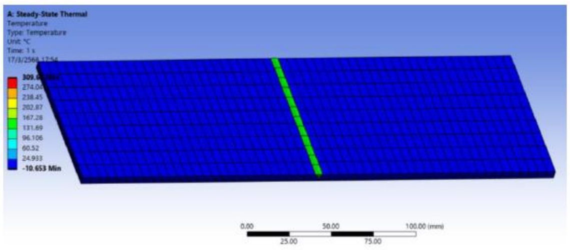

Figure 20 Temperature distribution obtained from numerical simulations

4. Conclusion

The main results for dissimilar welding between SS304 and Q245 steel using GTAW can be summarized as follows.

The microstructure in the weld metal zone consists of dendrite ferrite and austenite matrix. In addition, the results of the chemical composition examination using EDS technique found that many elements are components of the filler metal with chromium as the highest at 21.59%, followed by nickel at 10.17% in this weld metal zone.

The tensile test results showed that the stress-strain curves of the welded specimens were close to each other due to the fracture of the specimens resulting from the tensile test. However, all fractures were found to occur in the Q245 base metal, especially in the HAZ hot affected zone.

The hardness test found that the highest hardness value was in the heat effected zone (HAZ SS304) is 182 HV and the lowest hardness value was in heat effected zone (HAZ SS304). When the weld metal zone receives heat from welding, it changes its structure into a solid structure, which results in an increase in hardness value. In the welding process, the heat affected zone adjacent to the base metal will have a higher hardness value than the weld metal zone but higher than the base metal.

The accuracy of the temperature field with an infrared thermometer and numerical simulations gives temperature values that are not significantly different at 5% difference. This is due to the uneven cooling effect due to convection and radiation, resulting in a rapid decrease in the maximum temperature when the heat source passes through a certain location at a constant speed at the accumulated heat is transferred to the low temperature region of the plate by conduction and lost to the surrounding environment by radiation and convection.

The GTAW welding uses less energy than SMAW welding due to the lower heat consumption, but produces higher quality and cleaner results. Environmentally, GTAW welding has a lower impact than SMAW welding, particularly in terms of smoke and slag generation, making it more environmentally friendly.

5. References

[1] N. Jahanzeb, J.H. Shin, J. Singh, Y.U. Heo, S.H. Choi. (2017). Effect of microstructure on the hardness heterogeneity of dissimilar metal joints between 316L stainless steel and SS400 steel. *Materials Science and Engineering*, A007, 338-350.

[2] VJ Varghese, MR Suresh and DS Kumar. (2013). Recent developments in modeling of heat transfer during TIG welding-a review. *The International Journal of Advanced Manufacturing Technology,* 2013, 64, 749-754.

[3] Difference Box. (November 20, 2025). Difference Between SMAW and TIG Welding Processes. [Online], From: https://www.differencebox.com/engineering/difference-between-smaw-and-tig-welding-processes/

[4] H. Vashishtha, RV. Taiwade, S. Sharma, A.P. Patil. (2017). Effect of welding processes on microstructural and mechanical properties of dissimilar weldments between conventional austenitic and high nitrogen austenitic stainless steels. *Journal of Manufacturing Processes,* 25, 49-59.

[5] C. Li, G. Qina, Y. Tang, B. Zhanga, S. Lina, P. Gengb. (2020). Microstructures and mechanical properties of stainless-steel clad plate joint with diverse filler metals. *Journal of Materials Research and Technology*, 9, 2522-2534.

[6] M. Ghafouria, J. Ahnb, J. Mourujärvic, T. Björka, J. Larkiolac. (2020). Finite element simulation of welding distortions in ultra-high strength steel S960 MC including comprehensive thermal and solid-state phase transformation models. *Engineering Structures*, 219, 110804.

[7] I.R Ibrahim, M. Khedr, T.S. Mahmoud, H.A. Abdel-Aleem, A. Hamada. (2021). Study on the Mechanical

Performance of Dissimilar Butt Joints between Low Ni Medium-Mn and Ni-Cr Austenitic Stainless Steels Processed by Gas Tungsten Arc Welding. *Metals*, 11, 1439.

[8] C-H Huang, C-H Hou, T-S Hsieh, L. Tsai, C-C Chiang. (2022). Investigation of distinct welding parameters on mechanical and corrosion properties of dissimilar welded joints between stainless steel and low carbon steel. *Science Progress*,105, 1-8.

[9] M. Khedr, I. R Ibrahim, M. Jaskari, M Ali, H. A. Abdel-Aleem, T.S. Mahmoud, A. Hamada. (2023). Microstructural Evolution and Mechanical Performance of Two Joints of Medium-Mn Stainless Steel with Low- and High-Alloyed Steels. *Materials*, 16, 1624.

[10] J.Luijan, P. Surin, K. Eidhed. (2023). Investigation of ER308L and ER309L filler wires on dissimilar metals between carbon steel and 3CR12 ferritic stainless steel by GTAW through boiler fabrication in a sugar factory. *Materials Research Express*, 10, 1-4.

[11] Abdulrahaman Shuaibu Ahmad, Yunxin Wu, Hai Gong and Lin Nie Abdulrahaman Shuaibu Ahmad, Yunxin Wu, Hai Gong and Lin Nie. (2019). Finite Element Prediction of Residual Stress and Deformation Induced by Double-Pass TIG Welding of Al 2219 Plate. *Materials*, 12, 2251.

[12] S. Nuchim, P. Bunyawanichakul, N. Angsuseranee, V. Boonmag. (2025). Residual Stress and Distortion Analysis for TMCP Steel Grade EH36 Butt Welding Parts in GTAW-SMAW Hybrid Welding Process using Finite Element Method. *Engineering, Technology & Applied Science Research*, 15, 20077-20084.

[13] S. Baskutis, J. Baskutiene, R. Bendikiene, A. Ciuplys and K. Dutkus. (2021). Comparative Research of Microstructure and Mechanical Properties of Stainless and Structural Steel Dissimilar Welds. *Materials*, 14, 6180.